RESEARCH ARTICLE

WILEY

Effect of atmospheric stability on the dynamic wake meandering model applied to two 12 MW floating wind turbines

Irene Rivera-Arreba[1] | **Adam S. Wise**[2] | **Lene V. Eliassen**[3] |
Erin E. Bachynski-Polić[1]

[1]Department of Marine Technology, Norwegian University of Science and Technology, Trondheim, Norway

[2]Civil and Environmental Engineering, University of California, Berkeley, Berkeley, California, USA

[3]Department of Energy and Transport, SINTEF Ocean, Trondheim, Norway

Correspondence
Irene Rivera-Arreba, Department of Marine Technology, Norwegian University of Science and Technology, Trondheim, Norway.
Email: irene.rivera.arreba@ntnu.no

Funding information
Research Council of Norway, Grant/Award Number: 294573

Abstract

Current global analysis tools for floating wind turbines (FWTs) do not account for the combined effects of atmospheric stability and wakes from neighboring turbines. This work uses the mid-fidelity dynamic wake meandering model, together with turbulent wind fields generated based on stable, neutral, and unstable atmospheric conditions, to study the low-frequency content of the global responses of two semisubmersible FWTs separated by eight rotor diameters. Incoming wind fields based on the Kaimal spectrum and exponential coherence model, the Mann spectral tensor model, and a time-series input-based turbulence model are used. The respective input parameters for these models are fitted to high-fidelity large eddy simulation data.

In unstable, below-rated conditions, meandering leads to an increase in the yaw standard deviation of the downwind turbine of almost three times larger than the upwind turbine. Deficit and the upwards wake deflection affect the mean pitch and yaw, especially for the below-rated wind speed scenario. The mean pitch of the downwind turbine is reduced up to half the mean pitch value of the upwind turbine, whereas the mean yaw changes direction due to the enhanced effect of shear. The effect of meandering on the structural loading is highest on the standard deviation of the tower-top yaw moment of the downstream turbine, which increases more than 2.2 times compared to the upwind turbine value. Based on these findings, atmospheric stability affects wake deficit and meandering which in turn have a profound effect on the low-frequency global motions and structural response of floating wind turbines.

KEYWORDS
atmospheric stability, dynamic wake meandering, floating wind turbines, Kaimal, Mann, TIMESR

1 | INTRODUCTION

A substantial percentage of the world's offshore wind resource potential is found in deeper waters, where floating wind turbines (FWTs) are necessary. Since the wind field that a wind turbine encounters is directly affected by the neighboring turbines, the need to understand the effects of

wakes on FWTs is paramount. Wakes imply a decrease in mean wind speed, an increase in turbulence intensity and, as first observed by Ainslie,[1] they oscillate, or meander, both horizontally and vertically as they propagate. The characteristic meandering frequencies are low enough to be in the same frequency range as the natural frequencies of FWT rigid body motions. Several studies based on field data observations have reported non-neutral atmospheric conditions in the marine atmospheric boundary layer.[2-5] Ainslie[1] observed that wake meandering increased with decreasing atmospheric stability, which has been also reported by Churchfield et al.,[6] Keck et al,[7] or Abkar and Porté-Agel[8] in more recent studies. Furthermore, incoming wind fields in unstable atmospheric conditions are characterized by weak wind shear, high turbulence intensity, large coherent structures, and higher turbulence kinetic energy in the wake, while stable conditions are strongly sheared with very small coherent structures and lower turbulence intensity and kinetic energy and therefore slower recovery of wake. Consequently, not only does atmospheric stability affect the wake meandering but also the wind speed that a downwind turbine experiences.

The dynamic wake meandering (DWM) model was first proposed by Larsen et al[9] in 2008. Since 2019, the model has been included in the revised IEC 61400-1 standard[10] as a recommended practice to account for wake effects from neighboring turbines in a wind farm. This model is based on the hypothesis that the wake acts as a passive tracer driven by the large-scale turbulence structures in the atmospheric boundary layer. It has been developed for engineering applications and coupled to aero-hydro-servo-elastic tools such as HAWC2,[11] developed at DTU Wind and Energy Systems Department, and OpenFAST, developed by the National Renewable Energy Laboratory (NREL). The latter implements the DWM model as proposed by Larsen,[9] but with some differences, in FAST.Farm.[12] The DWM model[9] represents a compromise between accuracy and efficiency, and several works have aimed to validate it against experimental data or high-fidelity large-eddy simulation. Madsen et al[13] and Larsen et al[14] have validated the DWM model against operational wind farm measurement data, and Jonkman et al[15] and Doubrawa et al[16] have validated FAST.Farm against large eddy simulation, which have also been used to calibrate a number of wake dynamics parameters.[17] Kretschmer et al[18] validated the DWM model as implemented in FAST.Farm for the prediction of power output and structural loading in a single wake against measurements from the Alpha Ventus offshore wind farm. Wise and Bachynski[19] used the DWM model within FAST.Farm to study the effect of wake meandering on a semisubmersible, a spar and a TLP under neutral atmospheric conditions.

There are several studies on the response of floating wind turbines that either account for dynamic wake meandering or the effect of stability. In Rivera-Arreba et al,[20] the latter was studied for a single semisubmersible structure, the INO WINDMOOR 12 MW floating wind turbine.[21] To account for atmospheric stability, two sets of data were separately used: point measurements based on FINO-1[22] and LES data. For one single turbine, the structural responses are directly related to turbulence intensity and coherence, which are affected by atmospheric stability. However, wind turbines rarely stand alone, and the combined effect of dynamic wake meandering including atmospheric stability on the global motions and the structural response of a FWT has not previously been studied. In the current work, the effect of dynamic wake meandering, accounting for atmospheric stability, on the response of the INO WINDMOOR 12 MW semisubmersible floating wind turbine[21] placed eight rotor diameters (D) downstream in the wake is studied. To carry out the analyses, two semisubmersibles are modeled in OpenFAST 3.0[23] and FAST.Farm;[12] more details on the model set-up in FAST.Farm are included in Section 3. The incoming wind fields are realized using two different turbulence generators, TurbSim[24] and the Mann Turbulence generator,[25] based on the Kaimal and Mann synthetic turbulence models, respectively. The parameters of the synthetic models in which the previous wind generating methods are based depend on atmospheric stability.[26,27] These parameters are fitted to LES data, which are generated by the Weather Research and Forecasting (WRF) model's[28] LES capability under stable, neutral, and unstable atmospheric conditions. Additionally, the TIMESR model within TurbSim is used to generate the wind fields based on the time-series of the same set of high-fidelity LES data. Nine cases are studied, comprised of three stability conditions and three mean wind speeds at hub height, which cover a close-to-rated scenario, as well as a below-rated and an above-rated scenario in which the turbine operates with similar thrust levels. Six 3600 s realizations are performed for each case, accounting for a 1000 s transient, based on the findings of Kvittem et al,[29] where the convergence of fatigue estimates for different simulation length and number of simulations is investigated.

The current work is divided into the input wind field characteristics and the resulting wake deficit and meandering and the subsequent comparison of the structural response of the INO WINDMOOR 12 MW in the wake, with the same structure in free wind. Section 2 gives an overview of the DWM model and the wind turbulence methods used for the input of wind fields. Section 3 describes the set-up in FAST.Farm for the two INO WINDMOOR 12 MW semisubmersibles. Sections 4 and 5 analyze the wake meandering and deficit and their effects on the structural response of the floater under the conditions examined in this study.

2 | METHODOLOGY

2.1 | Environmental conditions

The significant wave height H_s and peak period T_p used in this work are consistent with the three chosen mean wind speeds (below-, close-to-, and above-rated) at hub height (HH). These conditions are determined based on the work of Li et al,[30] who defined a long-term joint distribution based on 10-year environmental hindcast data for a site in the Norwegian Sea with 200 m water depth (Site 14 in Li et al.[30]). The most likely significant wave height and peak period for the given and mean wind speeds U_w are retrieved in Table 1. Each environmental condition is studied for stable, neutral and unstable atmospheric stratification. To generate the ambient turbulent wind fields, the Kaimal, Mann, and TIMESR methods are used.

TABLE 1   Environmental conditions (EC) used in this work for the three mean wind speed scenarios.

	U_w (m/s)	H_s (m)	T_p (s)
EC1	7.5	2.3	8.3
EC2	12	2.9	8.4
EC3	16	3.5	8.6

2.2 | Dynamic wake meandering (DWM) model

The fundamental idea of the mid-fidelity DWM model is the splitting of turbulence scales based on a *cut-off eddy size*: Turbulent eddies smaller than this parameter influence the wake deficit evolution, whereas those larger than this size affect the wake meandering. This parameter is usually taken as 2 rotor diameters. Accordingly, the original model as proposed by Larsen et al[9] consists of three submodels:

1. **wake** (or velocity) **deficit**, described in the meandering frame of reference,
2. a stochastic model of the downstream **wake meandering** process and
3. the **added-wake turbulence** (or self-induced wake turbulence), described in the meandering frame of reference. The wake-added turbulence is not yet part of FAST.Farm.

The wake deficit evolution described in the meandering frame of reference is based on the thin shear-layer approximation of the Reynolds-averaged Navier-Stokes equations under quasi-steady-state conditions in axisymmetric coordinates, in the far-wake region, as

$$U\frac{\partial U}{\partial x} + V_r\frac{\partial U}{\partial r} = \frac{\nu_T}{r}\frac{\partial}{\partial r}\left(r\frac{\partial U}{\partial r}\right),$$ (1)

where U is the axial velocity component, V_r the radial velocity component, r the radial coordinate, and ν_T the eddy viscosity. The turbulence closure is modeled by an eddy-viscosity formulation. This approximation assumes that the velocity gradients are higher in the radial direction as compared to those in the axial direction. Furthermore, the pressure term is neglected. The eddy viscosity is modeled by the x dependent filter parameters F_{amb} and F_{shear}, described and calibrated by Madsen et al[13] and extended by Larsen et al[9] and Keck.[31] The eddy-viscosity $\nu_T(x,r)$ dependent on x and the radial position r as implemented in FAST.Farm is

$$\nu_T(x,r) = \nu_{amb}(x) + \nu_{shear}(x,r) =$$
$$= F_{amb}(x)k_{amb}TI_{amb}V_x\frac{D_{wake}}{2} + F_{shear}(x)k_{shear}\max\left\{\left(\frac{D_{wake}}{2}\right)^2\left|\frac{\partial V_x}{\partial r}\right|, \frac{D_{wake}}{2}V_{x,min}\right\},$$ (2)

where k_{amb} and k_{shear} are parameters that weigh the ambient and shear turbulence influence on the eddy-viscosity, V_x is the time-filtered disk average wind velocity normal to the actuator disk, TI_{amb} is the ambient turbulence intensity at each rotor, and D_{wake} is the wake diameter. In this work, the wake diameter is equal to the rotor diameter. The filter functions F_{amb} and F_{shear} depend on user-specified calibrated parameters. The ones used in this work are based on the work of Doubrawa et al.[16] The cut-off frequency of the low-pass time-filter for the wake advection, deflection, and meandering model is 0.2 Hz, based on the work by Branlard et al.[32] The DWM model as implemented in FAST.Farm does not include the added-wake model, which may impact the response of the wind turbine especially in low-ambient-turbulent conditions.[13] Furthermore, the mean and standard deviation of the wake deflection, as computed by the DWM model, are sensitive to the size of the polar grid, defined by the C_{meand} parameter used to calculate the spatial-averaged velocity with which the wake planes meander. In this work, the value for this parameter is the default one as defined in the FAST.Farm user manual, that is, $C_{meand} = 1.9$.

2.3 | Fit of the incoming wind fields to LES data

In this work, we use the LES capability of the WRF model[28] in its idealized configuration (where the initial conditions in terms of wind speed and temperature profiles are specified) to simulate the marine atmospheric boundary layer. This tool is a non-hydrostatic, fully compressible solver of the Euler equations including the Coriolis term. The base code is from WRF version 4.2.2, and modifications to the source code include a surface layer parameterization.[33] The LES data used to fit the synthetic wind field models and the TIMESR models extend over 1384 m and 232 m, in the y- and z-directions, respectively, and have 8.0 m resolution in both directions. This entire wind field is divided in six smaller wind fields in

the y-direction, which comprise the six seeds used to fit the synthetic and TIMESR models. This means that 6 two-dimensional planes are extracted from the LES, each with 29 points in the transverse direction and 30 points in the vertical direction. With a grid resolution of 8.0 m, this results in six 232 m $\times$ 240 m planes spanning the entire rotor swept area. The details on the LES set-up can be found in previous work.[20]

For each scenario and model, the six turbulent wind fields extracted from LES data are 1-h duration, as so are the wind fields generated by the Kaimal, Mann and TIMESR models. These 1-h wind fields are used to fit turbulence intensity, wind shear, spectral density, and coherence, described in the following.

Turbulence intensity TI is defined as

$$TI = \frac{\sigma_u}{\bar{u}_{hub}}, \tag{3}$$

where $\bar{u}_{hub}$ is the mean wind speed longitudinal component at hub height and σ_u the standard deviation of the same component.

Coherence gives information about the spatial variation of turbulence in the frequency space. Coherence γ of two spatially separated processes i and j, as a function of frequency, is defined as

$$\gamma_{i,j} = \frac{C_{i,j}}{\sqrt{P_i P_j}}, \tag{4}$$

where P_i and P_j are the power spectra of the two time-series separated by a specific lateral or vertical distance and $C_{i,j}$ is the cross spectrum between these two time-series. The real part of the coherence, $\text{Re}[\gamma_{i,j}]$, is known as co-coherence, whereas the imaginary is the quad-coherence.

The mean wind shear profile used in this work is based on the power-law equation, which defines the mean wind speed $\bar{u}$ at a certain height z as

$$\bar{u}(z) = \bar{u}_{ref} \left(\frac{z}{z_{ref}} \right)^{\alpha}, \tag{5}$$

where $\bar{u}_{ref}$ is the wind speed at a reference height z_{ref} and α is the power-law exponent. The α exponent is defined as a bulk parameter that includes both the effect of surface roughness z_0 and atmospheric stability.[34,35] This exponent is computed as the average of the fit at every point in y to the LES data. The shear exponents, which increase with increasing stability, are shown in Table 4.

2.3.1 | Kaimal spectrum and exponential coherence model (*Kaimal*)

The Kaimal spectrum with exponential coherence model[36] is based on the Kaimal spectrum in the three components. The IEC 61400-1 standard[10] accounts for coherence in the longitudinal direction. To include coherence in the three components, a model based on Davenport's coherence model,[37] based on an empirically fitted exponential decay, is usually applied:

$$\gamma_{i,j}(\delta, f) = \left[\exp\left(-a_K \sqrt{\left(\frac{f\delta}{\bar{u}_{hub}} \right)^2 + (\delta b_K)^2} \right) \right]^2, \tag{6}$$

where δ is the separation distance between time-series i and j of the K component, f is the frequency in Hertz, a_K the coherence decrement parameter, and b_K the coherent offset parameter. In the current work, the coherence parameters for the Kaimal model are obtained by fitting Equation (6) to the LES data, where δ is 24 m. The choice of δ is based on previous work.[20] Table 4, the top part, shows the coherence parameters a_K and b_K for the nine scenarios. The mean value for every parameter of the six realizations for each condition is used as input to TurbSim.[24]

The Kaimal model in TurbSim produces time-dependent wind in 2D planes and uses Taylor's hypothesis of frozen turbulence[38] to extend it into a third dimension. The height of the turbulence box is 600 m, and the width is 1304 m; there are 76 grid points in z and 164 grid points in y, and the resolution in z and y is 8 m. The time step is 0.1 s, and for every condition, six turbulent wind fields of 3600 s duration are generated. The IEC 61400-1 standard,[10] based on neutral atmospheric conditions, suggests that the standard deviation of the lateral wind speed component σ_v is 0.8 times the standard deviation of the longitudinal one σ_u, whereas the vertical one σ_w is suggested to be $0.5\sigma_u$. However, the relationship between the standard deviation of the three components in this work was found to vary depending on the atmospheric stability condition in the LES, as shown in Table 2. To account for these relationships, the corresponding line of TurbSim source code was modified.

2.3.2 | Mann spectral tensor model (*Mann*)

The three-dimensional spectral tensor model developed by Mann[39] requires three input parameters, which account for a certain degree of turbulence and a specific turbulence spectrum. The length scale L describes the size of the energy-containing eddies, and therefore, it decreases with atmospheric stability. The shear distortion parameter Γ defines the eddy-lifetime and the turbulent kinetic energy parameter $\alpha\epsilon^{2/3}$ accounts for the viscous dissipation rate. The model is based on mass and momentum conservation and uniform mean shear and is applicable for homogeneous turbulence under neutral atmospheric stability conditions. Since the model assumes shear generated turbulence, it does not include turbulence generated by buoyancy. The IEC 61400-1 standard recommends specific values for the three input parameters under neutral atmospheric conditions, which are derived from a fit to the Kaimal spectrum. However, since this work investigates the effect of atmospheric stability, the Mann model parameters are fitted to the LES data generated under stable, neutral, and unstable atmospheric conditions. To fit the parameters, the Matlab function *fitMann* from E. Cheynet[40] is used. The spectra of the 870 points generated in LES are estimated using Welch's algorithm[41] with a Hamming window, six segments, and 50% overlapping, following previous works.[2,42] Further, the spectra are bin averaged before the fitting is performed. Figure 1 shows the mean of L, Γ, and $\alpha\epsilon^{2/3}$ (A, B, and C, respectively) parameters at every height available from the LES data, that is, from 8 to 248 m, plus-minus one standard deviation for every height, indicated by the shaded area. These results correspond to the above-rated wind speed scenario. The horizontal black solid line represents the hub height, at 131.7 m, and the dashed lines the upper and lower bounds of the rotor. It is seen from Figure 1 that L increases with decreasing stability, as expected. The shear distortion parameter Γ increases with stability, as reported by Chougule et al,[43] based on measurements at Høvsøre. The trend of energy dissipation rate parameter $\alpha\epsilon^{2/3}$ depends on height. The derivative of the energy dissipation parameter with respect to height increases with decreasing stability. Coherence is intrinsic to the Mann model, since it is given by the integral of the spectral tensor itself.

In this work, the Mann model parameters are fitted at hub height; since there is not a grid point exactly at hub height, the parameters are linearly interpolated from the obtained parameters at the neighboring points above and below the hub height. The three-dimensional static wind boxes based on the Mann model are generated in the Mann 64-bit turbulence generator.[25] To move the respective wind boxes along the domains, Taylor's hypothesis of frozen turbulence is applied. The wind fields have 128 points in z, 256 points in y, and 16,384 points in x-direction, with a resolution in z and y of 8 m; in the x-direction, the spatial resolution depends on the mean wind speed at the reference height of the grid, which is defined at half the grid. In the current case, the reference height lies at 513 m. For the three wind speed scenarios analyzed in this work, dx varies from 1.875 m to 4 m, which yields a time step of 0.25 s, for every condition, based on Taylor's hypothesis. Six turbulent wind fields of 4096 s duration are generated for each scenario. Prior to applying the generated wind fields in FAST.Farm, the Mann turbulence

TABLE 2 Relationship between the standard deviation of the wind speed longitudinal, lateral, and vertical components, σ_u, σ_v, and σ_w, based on LES.

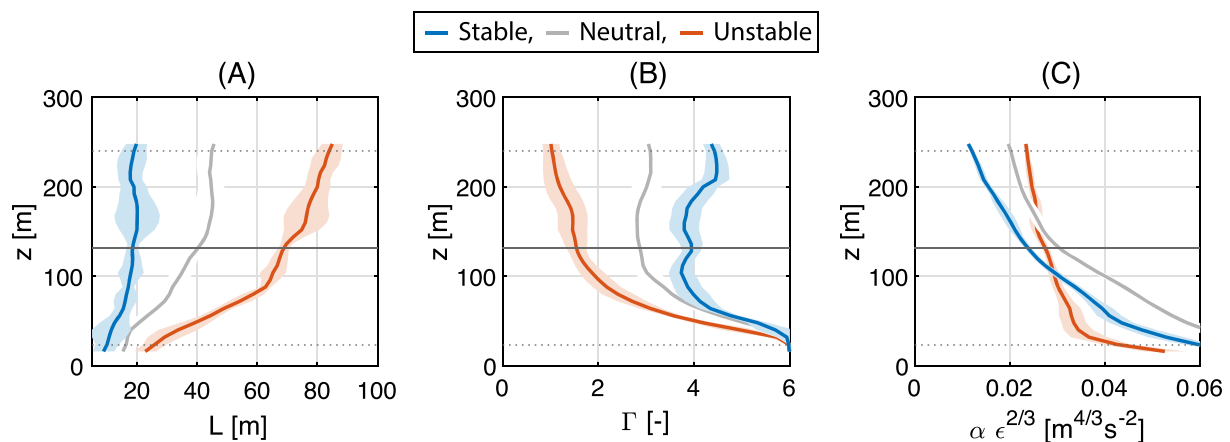|	
Stable conditions	$\sigma_v = 0.7\sigma_u$; $\sigma_w = 0.5\sigma_u$
Neutral conditions	$\sigma_v = 0.8\sigma_u$; $\sigma_w = 0.6\sigma_u$
Unstable conditions	$\sigma_v = 1.1\sigma_u$; $\sigma_w = 0.9\sigma_u$

FIGURE 1 Mann model parameters fitted to LES data for the above-rated wind speed scenario in stable, neutral, and unstable atmospheric conditions, as a function of height. The colored solid lines show the average at every height, plus-minus one standard deviation, represented by the shaded area. (A) Length-scale parameter L, (B) shear distortion parameter Γ, and (C) energy dissipation rate parameter $\alpha\epsilon^{2/3}$. The solid horizontal line outlines the hub height, whereas the dashed lines represent the rotor limits.

wind boxes are scaled to match the standard deviation for each scenario based on the high-fidelity data. A summary of the spatial and temporal resolution of the turbulent wind fields is presented in Table 3.

2.3.3 | TIMESR

The third method used in the current work to generate the input turbulent wind fields is the TIMESR model, a capability within TurbSim. This method uses directly the spectral amplitudes of an input time-series, which are linearly interpolated in the specific domain if no points from the input time-series are available. In the current case, the time-series input is the six realizations of LES data for each environmental condition and atmospheric stability; these data cover 870 points distributed over the rotor area. Therefore, the output of this wind field generating method corresponds to the closest one to the LES data, if compared to Mann and Kaimal. Coherence is included by modifying the phases of the generated time-series, based on Veers' method.[44] Davenport's coherence model, based on an exponential function with a decay parameter C_K, is used as

$$\gamma_i(\delta, f) = \exp\left(-C_K \frac{f\delta}{\bar{u}_{hub}}\right). \tag{7}$$

To obtain the decay parameters for the three wind speed components, C_u, C_v, and C_w, the exponential function is fitted to the LES data. The fitted parameters are presented in Table 4. Similar to the characteristics of the Kaimal wind boxes, the height and width of the turbulent wind fields are 600 m and 1304 m, with 76 and 164 points, respectively. The resolution in z and y is 8 m, and the time step is of 0.1 s, as presented in Table 3.

2.4 | Spectral density and coherence of the generated wind fields

Figure 2 shows the standard deviation at the grid point closest to the hub, for the three mean wind speeds, the three stability conditions, and the three models. The solid markers represent the mean value of the six realizations for every scenario and wind model, whereas the transparent markers correspond to the different realizations. The black triangles show the target values, based on the mean of the six seeds of the LES data

TABLE 3 Spatial and temporal discretization of the turbulent wind fields generated by Kaimal, Mann, and TIMESR.

	dy (m)	Ny	dz (m)	Nz	dt (s)	T (s)
Kaimal	8	164	8	76	0.10	3600
Mann	8	256	8	128	0.25	4096
TIMESR	8	164	8	76	0.10	3600

TABLE 4 Coherence parameters a_K and b_K of the Kaimal model and Davenport coherence model parameters C_K.

	Stable			Neutral			Unstable		
	7.5 m/s	12 m/s	16 m/s	7.5 m/s	12 m/s	16 m/s	7.5 m/s	12 m/s	16 m/s
a_u	1.90	3.32	4.15	1.27	2.64	4.15	1.47	2.55	3.15
b_u	$-2.09 \cdot 10^{-3}$	$-1.39 \cdot 10^{-4}$	$7.02 \cdot 10^{-4}$	$-1.06 \cdot 10^{-3}$	$5.61 \cdot 10^{-4}$	$3.63 \cdot 10^{-5}$	$2.49 \cdot 10^{-6}$	$7.37 \cdot 10^{-7}$	$3.59 \cdot 10^{-4}$
a_v	0.46	1.58	1.99	0.97	1.64	2.32	1.10	1.65	2.24
b_v	0.04	0.02	0.01	$7.74 \cdot 10^{-3}$	$3.71 \cdot 10^{-3}$	$2.98 \cdot 10^{-3}$	$-1.80 \cdot 10^{-3}$	$2.02 \cdot 10^{-3}$	$7.64 \cdot 10^{-4}$
a_w	0.75	1.31	1.44	0.56	0.92	1.18	0.46	0.82	1.00
b_w	0.01	$7.99 \cdot 10^{-3}$	$7.64 \cdot 10^{-4}$	$3.87 \cdot 10^{-4}$	$5.23 \cdot 10^{-3}$	$3.39 \cdot 10^{-3}$	$-1.8 \cdot 10^{-3}$	$-1.4 \cdot 10^{-3}$	$2.03 \cdot 10^{-3}$
C_u	4.95	10.00	12.49	3.43	6.47	9.41	3.14	5.74	7.46
C_v	7.66	17.22	18.83	2.76	4.75	7.30	2.40	4.00	6.35
C_w	2.23	4.58	6.16	1.25	2.40	3.46	0.95	1.77	2.36
α [-]	0.146	0.183	0.144	0.070	0.076	0.075	0.019	0.024	0.028

Note: The bottom-most row indicates the α shear exponent parameter from the power-law shear model.
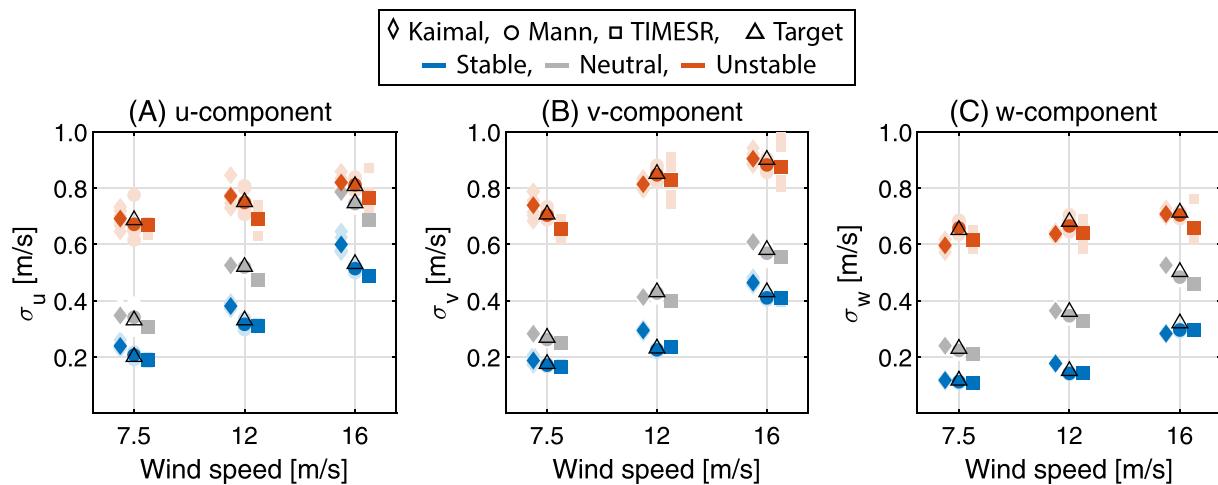
FIGURE 2 One-hour averaged standard deviation of the u- (A), v- (B), and w- (C) components at hub height, for the three stability conditions, models and wind speed scenarios. In this figure, and in other subsequent ones with the same x-axis, the results are separated slightly in the x-direction for better readability.

for each scenario, computed as the average over the rotor span, that is, the average over the 29 points along the y-direction over the rotor. These target values follow the relationship shown in Table 2. The wind field generated based on the TIMESR method coincides with that of the LES data, at the points where data are available. The Mann model standard deviation is scaled to match the target value. The Kaimal and TIMESR models are seen to have very close values to the target ones, except for specific cases in stable and neutral conditions, for which the Kaimal model overestimates the standard deviation with respect to the TIMESR model. The reason for this overestimation is the higher energy content at higher frequencies that the Kaimal method implies, compared to the TIMESR model.

Figure 3 presents the power spectral density (PSD) of the three wind speed components for the three stability conditions, for the below-rated wind speed scenario, for the three models (Kaimal, Mann, and TIMESR), in colored lines, and for the LES data, outlined by a solid black line. The PSD for Mann, Kaimal, and TIMESR is computed as the average of the six seeds at seven points distributed over y, at hub height. The seven points are at $y = 0, 4, -4, 60, -60, 108,$ and -108 m, and they are indicated in Figure 4 by white solid lines, along the entire domain; the average at these seven points is the result presented here. For the LES data, the black line shows the average of the PSD at the seven points. The energy content of the TIMESR and LES models decreases for frequencies above approximately 0.1 to 0.2 Hz due to the grid resolution in the LES data, whereas Mann and Kaimal continue to cascade at the $-5/3$ power-law. This decrease in energy content for the TIMESR model above approximately 0.2 Hz, together with the lower energy content at lower wind speeds, yields the decrease in standard deviation that is seen for stable and neutral conditions, compared to the Kaimal model. In unstable conditions, for the lateral and vertical wind speed components, the energy content at the lower frequencies in the case of TIMESR is higher. Furthermore, the longitudinal component shows a higher energy content at 0.003 Hz, which is related to a characteristic size of $\bar{u}_{hub}/f = 2500$ m for the convective cellular structures resolved in the LES data,[45] for a mean wind speed of 7.5 m/s. Figure 4 shows the instantaneous, undisturbed, flow of the u-component at hub height, at $t = 0$, for Kaimal, Mann, TIMESR, and the LES data, for unstable conditions, and one seed. For the TIMESR and LES models, the structures, or eddies, corresponding to the 0.003 Hz frequency, are present. The characteristic sizes of the convective cellular structures are rooted in physics but can depend on numerics. Cellular structures are common in unstable or convective atmospheric boundary layers. These structures are qualitatively evident in multi-kilometer radar observations (see fig. 2d from Hirth et al.[46]) and satellite images (fig. 1 from Göcmen et al.[47]).

Figure 5 shows the average lateral co-coherence (over six seeds) for the three wind speed components, for the below-rated scenario, top row, and the above-rated scenario, bottom row, for a distance δ_y of 1 D, as a function of the reduced frequency ($f_r = f\delta_y/U_w$). In general, coherence tends to zero as frequency increases. The generally higher coherence under unstable conditions for the lowest frequencies, or wave numbers, is consistent with the larger eddy size. The TIMESR model based on the LES data input and the Kaimal model show the highest coherence. The Mann model has the lowest coherence for the longitudinal and vertical wind speed components. For the transverse wind speed component, for the stable and neutral conditions, coherence of the Mann model is higher than the one for Kaimal. The trends seen for the rated wind speed scenario, or for a separation of 0.5 D, are similar to those described here. The results are based on two points within the rotor area, chosen to be representative when analyzing the global motions and structural responses. From Figure 4, the higher lateral coherence for the longitudinal component of the wind speed in unstable conditions is qualitatively very clear, as well as the higher coherence for the TIMESR model, and the lowest one for the Mann model.
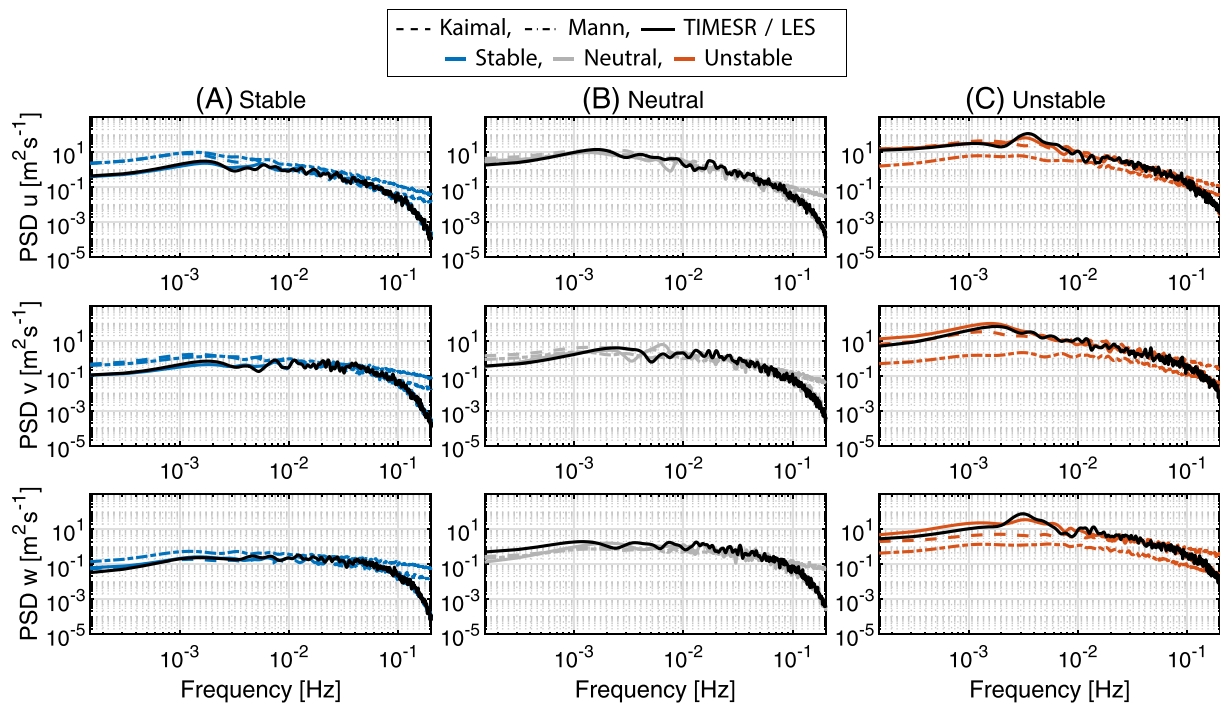
FIGURE 3 Averaged PSD over seven points along y at hub height, and six seeds for the Kaimal, Mann, and TIMESR models, of the u-, v-, and w-components for the below-rated wind speed scenario, for the three wind models and stable (A), neutral (B), and unstable (C) conditions. The black solid lines represent the LES data: It overlaps in general the average of the seeds for the TIMESR model, which is outlined by the colored solid line, respectively for each stability condition.
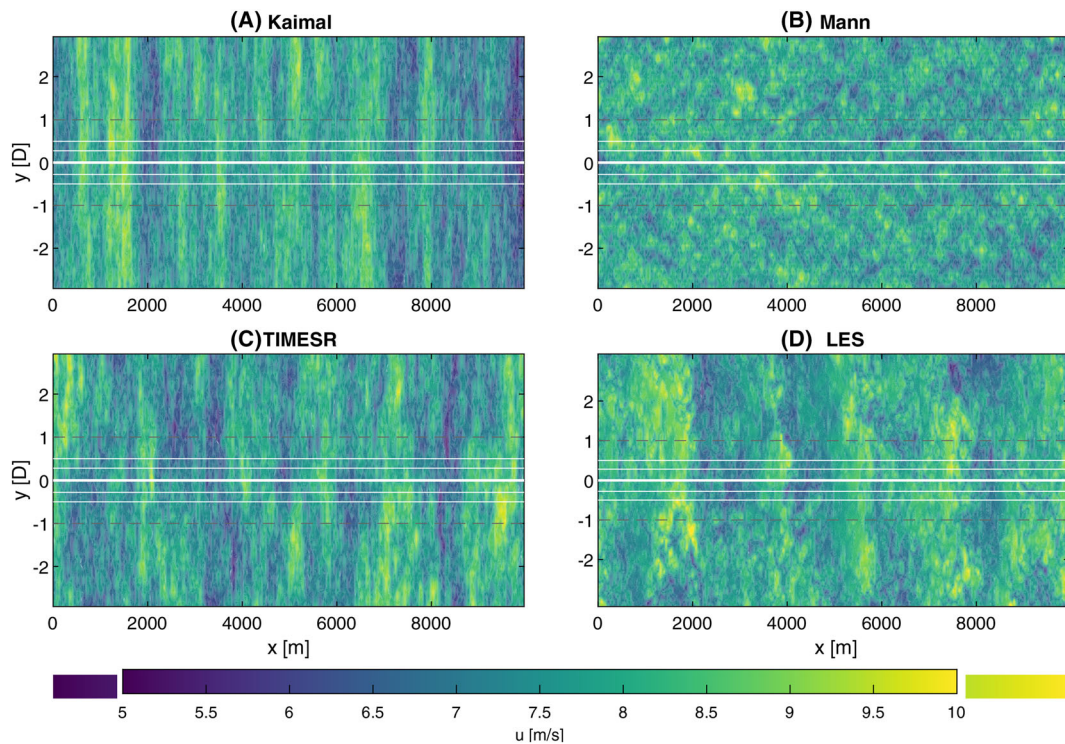

FIGURE 4 Top-view of the instantaneous flow visualization at t=0 of the u-component in unstable conditions for the Kaimal (A), Mann (B), TIMESR (C), and LES (D) models, for the below-rated wind speed scenario. The dashed black lines indicate the borders of the transverse wake meandering, and the white solid lines indicate the seven points used to compute the PSD of the wind speed at hub-height.

3 | NUMERICAL SET-UP

The INO WINDMOOR 12 MW semisubmersible FWT, shown to the right in Figure 6, is used to study the effect of atmospheric stability on the FWT under wake effects. The semisubmersible has three columns connected by three upper and three lower pontoons. The tower is installed on top of one of the columns. The mooring system consists of three hybrid (chain and polyester) catenary mooring lines. A more comprehensive description of the INO WINDMOOR 12 MW and its mooring system are provided by Silva de Souza et al.[21] Table 5 presents the main characteristics of the wind turbine. The natural frequencies of the six rigid modes of the platform, together with the 1P rotating frequency at rated wind speed and the first tower fore-aft bending frequency, are given in Table 6. A controller with motion compensation is used, based on the work of Silva de Souza and Bachynski-Polić,[48] where the specific details on the control system can be found.

FAST.Farm is used to study the effect of atmospheric stability on the structural response of the INO WINDMOOR 12 MW in the wake. The numerical domain, sketched in Figure 6A, is almost 10 km long, 1272 m wide, and 600 m high. Within this volume, two sub-domains are specified: the low-resolution domain, whose dimensions coincide with the entire domain, and the high-resolution one. Turbine 1 (indicated as T1) is placed at x = 240 m, and turbine 2 (T2) at x = 1975.2 m. The rectangular areas over T1 and T2, which are 250 m wide and high and 525 m long, expressed in rotor diameters in Figure 6A, represent the high-resolution domains. The resolution of each domain is presented in Table 7, where dSLow is the resolution in both y- and z-directions in the low-resolution domain, and dSHigh the corresponding one in the high-resolution domain. The time steps for both domains, DtLow and DtHigh, are indicated in Table 7, which includes the recommended values based on the

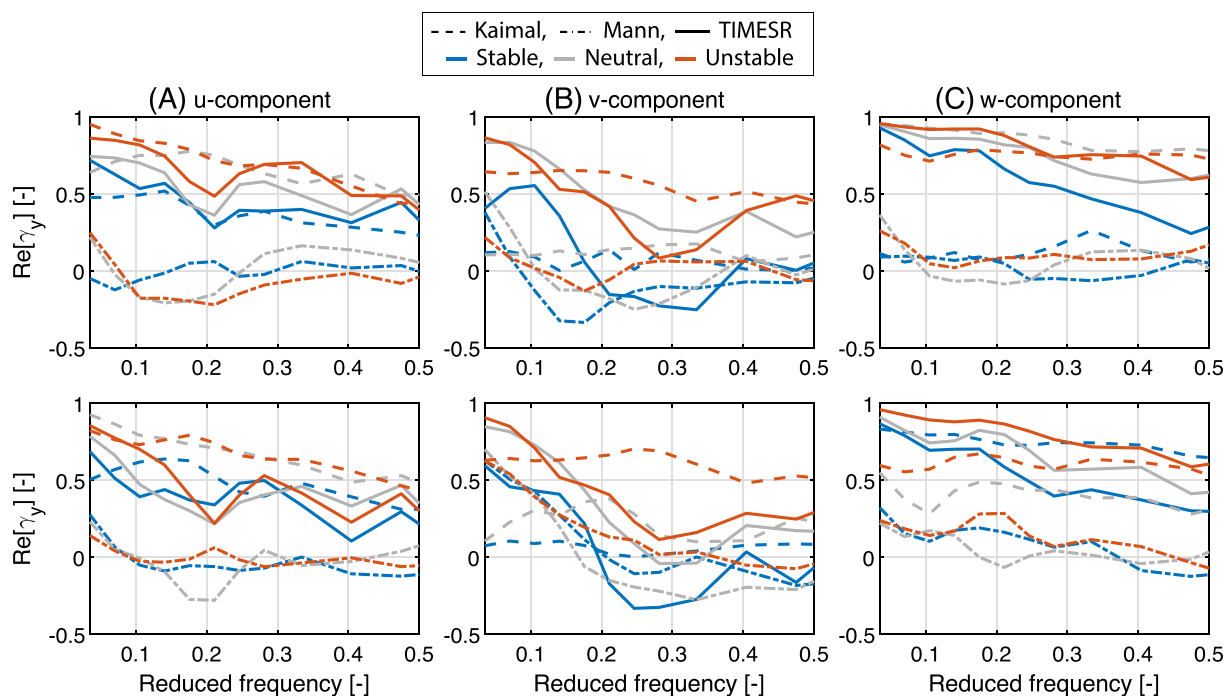**FIGURE 5** Lateral co-coherence of the u- (A), v- (B), and w- (C) components, for two points at a separation distance of 1D for the below-rated (top row) and the above-rated (bottom row) wind speed scenarios.
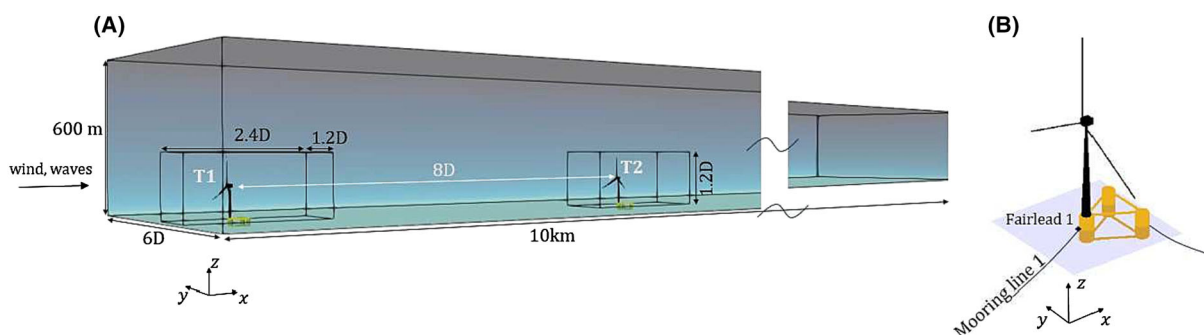

FIGURE 6 (A) FAST.Farm high- and low-resolution domains, with the former truncated, and (B) geometry of the INO WINDMOOR 12 MW model.

TABLE 5 INO WINDMOOR 12 MW wind turbine main characteristics.

Rotor diameter	Cut-in, rated, cut-out wind speed	Cut-in, rated rotor speed
216.9 m	4 m/s, 10.6 m/s, 25 m/s	5.5 rpm, 7.8 rpm

TABLE 6 Platform natural frequencies in OpenFAST.

Degree of freedom	Surge	Sway	Heave	Roll	Pitch	Yaw	1P	1st FAB
Frequency (Hz)	0.011	0.011	0.062	0.035	0.033	0.013	0.130	0.641

Abbreviations: 1P, rated rotor frequency; FAB, tower fore-aft bending frequency.

TABLE 7 Recommended and applied values for the spatial and time resolution in the FAST.Farm set-up.

		Applied (Recommended)		
	Recommended	7.5 m/s	12 m/s	16 m/s
dSLow (m)	$< \frac{C_{meander} D_w U_w}{150 m/s}$	24 (<21)	32 (<33)	40 (<44)
dxHigh (m)	-	0.75	1.2	1.6
dSHigh (m)	$< c_{max}$	8	8	8
DtLow (s)	$< \frac{C_{meander} D_w}{10 U_w}$	2.5 (<5.5)	2.5 (<3.4)	2.5 (<2.6)
DtHigh (s)	-	0.025	0.025	0.025

$C_{meander} = 1.9$.
$D_w = D_{rotor}$.

FAST.Farm manual[49] (Recommended) and the ones used in this work (Applied). The slightly higher value of dSLow for the below-rated wind speed scenario, compared to the recommended value to be lower than 21 m, is justified by the combination of aiming for a dSLow being a multiple of the high-resolution domain, that is, 8 m, and the following statement in the FAST.Farm manual: *It was found that the mean horizontal and vertical wake trajectories have negligible dependence of DtLow or DSLow*. The dSHigh value applied is also higher than the maximum blade chord length c_{max}, that is, 6.5 m; however, the focus of this study is not on the blade structure response itself, and the LES data available had a resolution of 8 m, and therefore, a slightly lower resolution was acceptable.

4 | RESULTS ON DEFICIT AND MEANDERING

Figure 7 shows the time-averaged wake deficit over the last 3600 s for one realization (or seed), for the TIMESR model, at a YZ-plane of the high-resolution domain, placed at 7.5 D downstream T1, that is, right in front of T2, which is at 8 D. The spatial dimensions are in rotor diameters, and the hub height is subtracted from the vertical position. Here, the deficit is defined as the ratio between the mean wind speed at 7.5 D, $u_1(y,z)$, and the undisturbed wind speed that encounters T1, $u_0(y,z)$. The columns show the deficit for stable, neutral, and unstable conditions (A, B, and C, respectively), whereas the rows, from top to bottom, correspond to the 7.5 m/s, 12 m/s, and 16 m/s wind speed scenarios. The initial position of the rotor under the different conditions is outlined by the black circles.

There are several ways of defining the wake center location, as described by Quon et al.[50] In this work, the center of the wake is computed as the weight center of the velocity deficit. From Figure 7, for the below-rated wind speed scenario, this center is half a diameter higher than the hub height, which implies that the wake deflects upwards. This phenomenon has been previously observed by Wise and Bachynski,[19] Doubrawa et al,[51] and Nanos et al,[52] for below-rated wind speeds. The reason behind this deflection is the non-zero vertical component of the thrust that the incoming flow experiences when encountering a rotor with a specific tilt with respect to the ground. This vertical component induces a vertical force in the wake, which results in an increased vertical component of the wind speed in the wake. Consequently, the wake deflects upwards for the below-rated wind speed scenario. The mean vertical deflection shown in this case is for a grid size meandering parameter, C_{meand}, based on the findings of Larsen et al,[9] that is, the recommended value in the FAST.Farm manual. However, this value needs to be adjusted on a case-to-case basis, as reported by Rivera-Arreba et al,[53] accounting for both lateral and vertical meandering. For the close-to-rated and above-rated wind speed scenarios, there is a smaller ratio between the vertical and longitudinal components of the wind speed. As wind speed increases, so does the longitudinal component of the wind speed. However, the induced vertical component remains the same, which results in a smaller w-to-u ratio. This smaller ratio prevents the center of the wake from moving upwards. For the unstable case, at 7.5 m/s, Figure 7 shows that the
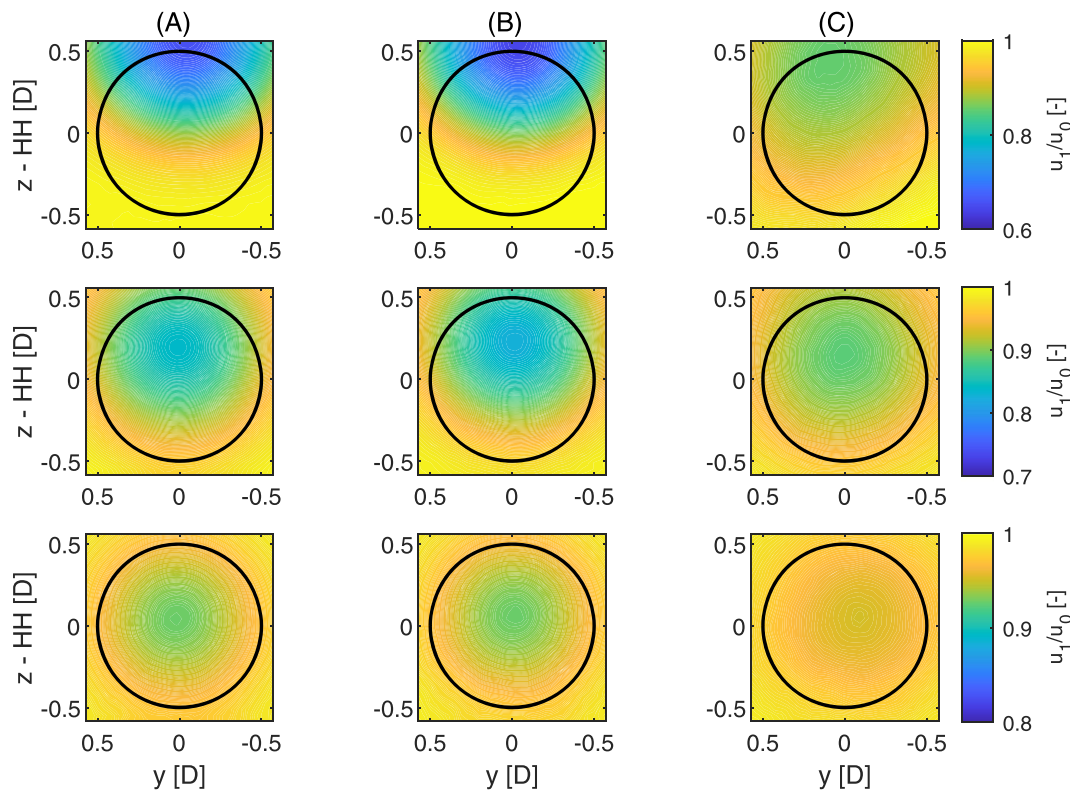
FIGURE 7 Time-averaged deficit at 7.5 D downwind T1, for the TIMESR model, and the 7.5 m/s (top), 12 m/s (middle), and 16 m/s (bottom) scenarios. Column (A) shows stable conditions, column (B) neutral conditions and column (C) unstable conditions.

wake deflects towards a positive y-direction. The non-zero mean of the transverse deflection is due to a higher meandering in unstable conditions. The direction and magnitude of this deflection varies from seed to seed, but its range is small, i.e. the mean deflection in y does not exceed 0.1 D. Furthermore, the deficit at the center of the wake is seen to be smaller under unstable conditions. This higher rate of recovery for unstable conditions is expected, since turbulence is higher for these conditions. The same argument can be applied to stable and neutral conditions, since neutral conditions are characteristic to present higher turbulence in comparison. However, the deficit under these conditions is slightly larger than for stable conditions. The reason for the smaller deficit for stable conditions is related to the shear profile: for stable conditions shear is higher, and consequently, the difference in wind speeds with height is larger. This effect is enhanced for the below-rated scenario, under which the wake deflects upwards. The upward deflection of the wake results in the wake experiencing faster wind speeds for stable conditions compared to neutral ones, leading to a faster recovery of the wake. The wake recovery is quicker as the mean wind speed increases due to lower induction factors. The trends described here are seen for every model and realization.

Figure 8 shows the statistics of the lateral (y_c) and vertical center (z_c) position of the wake, measured at 7.5 D for the three models, in rotor diameters, for neutral and stable conditions. In the case of the vertical position of the wake, the hub height is subtracted. The reason for not presenting the statistics for the unstable conditions is that the mean value is equivalent to the stable and neutral conditions, and the standard deviation is sensitive to the method of tracking the wake center, that is, by computing the weight center of the velocity deficit. Instead, Figure 9 shows the PSD of the vertical and horizontal meandering in unstable conditions, for the three models and mean wind speed scenarios. The middle of the rectangles represents the average of the mean of the vertical or lateral meandering of the wake center, for the six realizations; the height of the rectangles is equal to two standard deviations, computed as the average of the standard deviations of the six realizations. The points over and below the box show the six maxima and minima, respectively, for each realization. For the stable and neutral conditions, the meandering for the three models shows a similar mean and standard deviation of the wake center position, both laterally and vertically. The slightly larger lateral meandering for TIMESR can be explained by the lower lateral co-coherence, as seen from Figure 4; even though the vertical co-coherence is not shown, the same reasoning applies to the larger vertical meandering in unstable conditions for TIMESR.

The lateral and vertical positions of the wake center meander the most in unstable conditions, due to larger coherent structures. Furthermore, meandering is the largest for the below-rated wind speed scenario. For this scenario, a few non-physical spikes (below sea level) in the wake center output were removed of the time series, and replaced by a linear interpolation from the immediately previous and following values. The PSD of the wake center meandering in unstable conditions presented in Figure 9 shows a lower energy content as the mean wind speed increases, which is explained by the larger longitudinal component of the wind speed compared to the vertical or lateral one, with which the meandering of
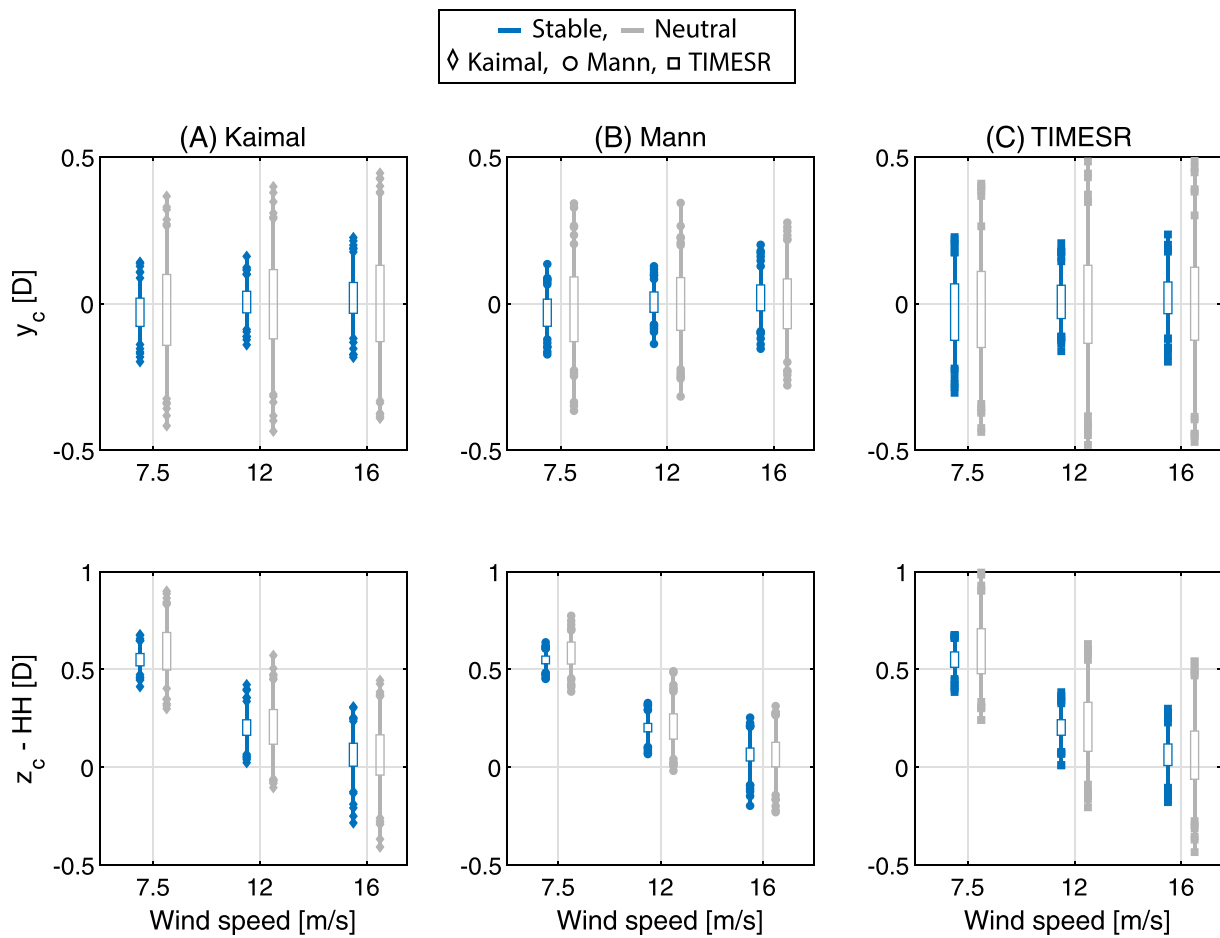
FIGURE 8 Statistics of the lateral (top) and vertical (bottom) position of the wake center for the six seeds, for neutral and stable atmospheric stability conditions and the three models: (A) Kaimal, (B) Mann, and (C) TIMESR. The mid-point of the rectangles is the mean and its height two standard deviations. The points represent the maxima and minima for the six seeds for each condition.
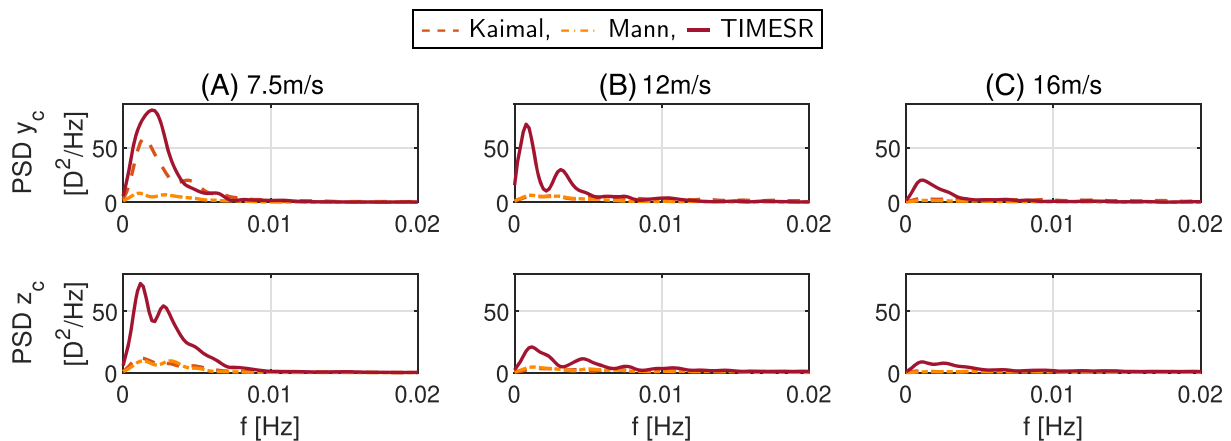

FIGURE 9 Average of the PSD over the six seeds for the lateral y_c (top) and vertical z_c (bottom) wake center at 7.5 D, for unstable conditions, for 7.5 m/s (A), 12 m/s (B), and 16 m/s (C), for the three models.

the wake is highly correlated. Due to a larger u-component of the flow parallel to the wake longitudinal advection, the wake cannot meander laterally and vertically as easily as when smaller longitudinal components are present. The TIMESR model presents a higher energy content for both lateral and horizontal wake meandering, which is consistent with the larger coherent structures, and with the higher energy content of the lateral and transverse components of the wind speed in unstable conditions for this model, compared to Mann and Kaimal.

5 | RESULTS ON GLOBAL MOTIONS AND STRUCTURAL RESPONSE

The most representative global motions, based on the conditions of the current work, are surge, pitch and yaw; heave, sway and roll are relatively small. Furthermore, due to the strong correlation between surge and pitch with thrust, the former is not presented in this work. In this section, the mean and standard deviation of platform pitch and yaw motions for both the turbine in the free wind (T1) and the turbine in the wake (T2) are presented, for the three turbulence models, the three stability conditions and the three mean wind speeds. Regarding the loading on the structure, the focus is on the mean and standard deviation of the tower base fore-aft bending moment (TBFABM), the tower top torsional moment at the yaw bearing (TTYM), the blade root out-of-plane moment (BROoPM) and the tension at fairlead 1 (FL1T). The position of fairlead 1 is indicated in Figure 6B.

5.1 | Global motions: pitch and yaw

Figure 10 presents the average of the mean values from each of the six realizations for the platform pitch (top row) and yaw (bottom row), represented by stars and triangles, plus-minus the average of the standard deviations for the six realizations, represented by the error bars, for each mean wind speed and stability condition, and for T1 and T2. Column (A) is for the Kaimal model, column (B) for the Mann model, and column (C) for the TIMESR model.

Compared to T1, T2 has a smaller mean pitch for the below-rated wind speed scenario due to a decrease in the wind speed, which yields a lower rotor thrust. For the 12 m/s wind speed scenario, that is, slightly above rated, the opposite occurs: The reduced wind speed at T2 implies an increase in thrust. For the above-rated wind speed, the wake recovery is higher, and therefore, the wind speed at T2 is very close to the mean undisturbed incoming wind speed that T1 encounters. Consequently, the thrust that T1 and T2 experience is very similar. The influence of the wind turbulence models and atmospheric stability on the mean pitch is minor, with a maximum difference of $1.3°$ between T2 and T1, for the below-rated wind scenario and neutral and stable conditions, and an increase of 15% for neutral and stable conditions, for the close-to-rated scenario. It can thus be inferred that the mean pitch of the turbine in the wake is mainly affected by the wake deficit. The difference between T1 and T2 pitch standard deviations is negligible for the above-rated wind speed scenario, for any condition and wind turbulence model. For the
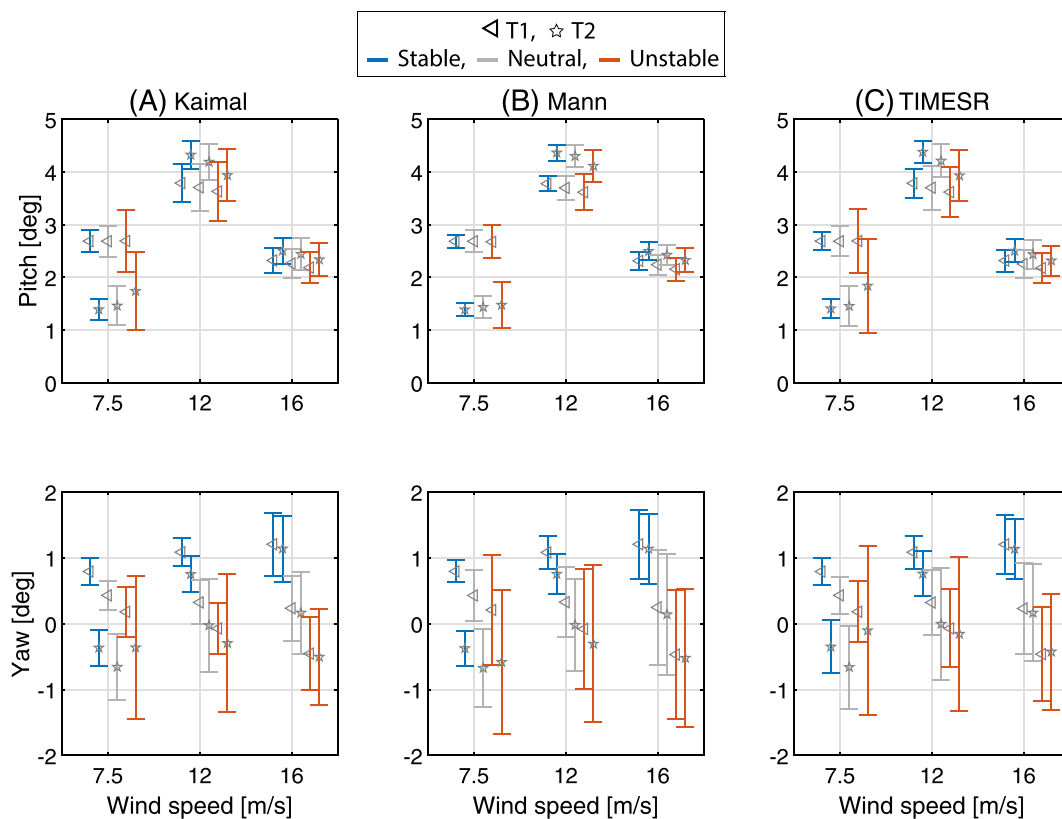

FIGURE 10 Average of the mean of the six realizations for pitch (top row) and yaw (bottom row), plus-minus the average of the standard deviation for the six realizations, for each mean wind speed and stability condition, and for T1 (triangle markers) and T2 (star markers). Column (A) is for the Kaimal model, column (B) for the Mann model, and column (C) for the TIMESR model.

below-rated scenario, the maximum difference in standard deviation is seen for the Kaimal and TIMESR models, in unstable conditions: in this case the standard deviation for T2 is 1.2 and 1.4 times the standard deviation of T1, respectively. This difference is lower for the Mann model. For stable and neutral conditions, the maximum difference in standard deviation is approximately a 30% decrease for the close-to-rated case, in both conditions, for TIMESR and Kaimal. The standard deviation in pitch is mostly affected by turbulence intensity and wake meandering, which is highest in unstable conditions, for the below-rated wind speed scenario, and the TIMESR model.

The difference in the mean yaw between T1 and T2 is more pronounced for the below-rated wind speed scenario and for neutral and stable conditions. The mean yaw for T1 shows a different behavior in stable compared to unstable conditions. In stable conditions, it increases positively with increasing wind speed, whereas for unstable conditions it increases in the negative direction with increasing wind speed. This difference is caused by the increased shear for stable conditions, as shown in Figure 11. The higher shear in stable conditions results in a more pronounced asymmetric loading on the blades. This asymmetry yields an increased aerodynamic moment around the y- and z-axes, which causes the structure to rotate in yaw and displace in sway in the positive direction. Figure 11 illustrates the cause of this phenomenon by showing the mean yaw and sway of T1 for constant wind, for different shear levels. The respective shear exponents α used in this case for stable, neutral and unstable, are 0.14, 0.07 and 0.02. For a shear exponent typical for stable conditions (in blue), yaw increases with mean wind speed, whereas for no shear at all (black), which would be close-to unstable conditions, the mean yaw decreases as wind speed increases. Figure 10 shows that the difference in absolute value between the mean yaw for T1 and T2 for the below-rated wind speed scenario is relatively small, with a maximum value of approximately 0.4° in stable conditions, and the three models. The mean yaw for T2 has a different direction than T1 in stable and neutral conditions for the below-rated wind speed scenario, due to the wake deflection upwards. This deflection results in the lower part of the rotor experiencing larger wind speeds than the upper part, as depicted in the top, left (A), in Figure 7. As a result of this *inverse* shear, the direction of the mean yaw angle for T2 differs from that of T1. For unstable conditions, below-rated, the difference between T1 and T2 is negligible. For the above-rated wind speed scenario, the mean values for T1 and T2 are almost equal, due to a smaller deficit. For the cases shown here, the mean yaw of T1 is sufficiently small to not show any influence on the transverse deflection of the wake.
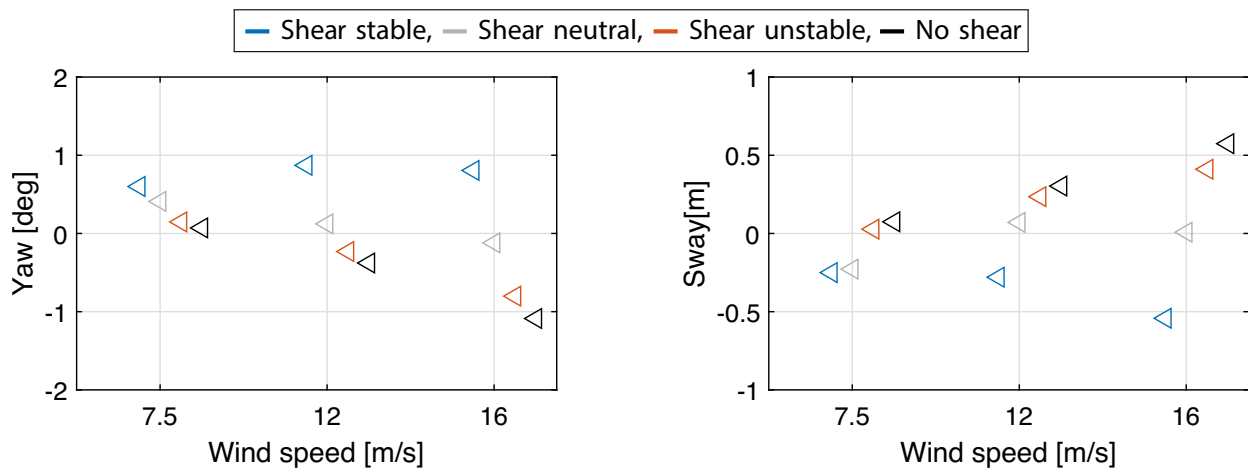

FIGURE 11   Effect of shear on the mean yaw and sway for T1 for below-, close-to-, and above-rated constant wind conditions.
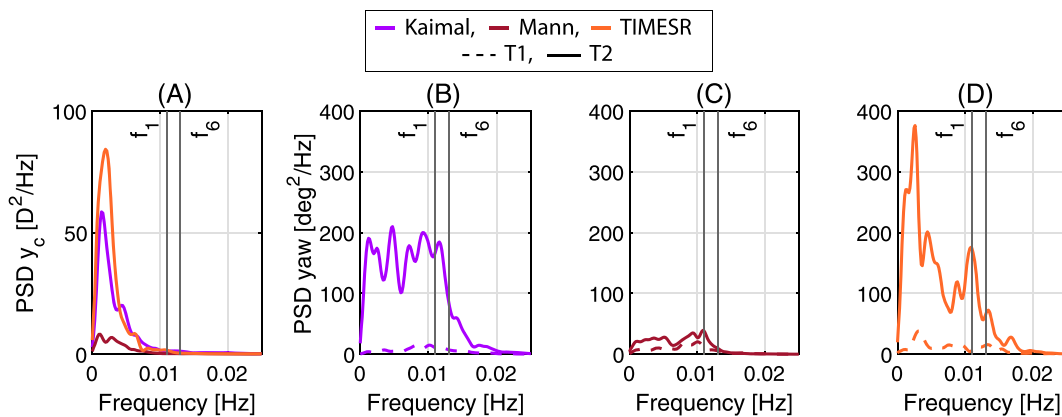

FIGURE 12   (A) PSD of the average of the six seeds for the wake center lateral meandering y_c, for the below-rated scenario. (B, C, and D) PSD of the yaw for T1 and T2, for (B) Kaimal, (C) Mann, and (D) TIMESR. All the PSDs are for unstable conditions.

The maximum absolute difference in the standard deviation in yaw between T1 and T2 is almost $1°$ and occurs for the below-rated wind speed scenario for unstable conditions, for the TIMESR model. Although the absolute values are small, for the below-rated scenario, the standard deviation in yaw for T2, for unstable and neutral conditions, reaches between almost two and three times the one of T1, for both the Kaimal and TIMESR models. The cause for a generally larger standard deviation in yaw for the turbine in the wake, T2, in unstable conditions, is the increased meandering, as seen from Figure 12, where the PSD of the lateral meandering of the wake center is presented (A), together with the spectra for the three models (B, Kaimal; C, Mann; and D, TIMESR), for unstable conditions, and the below-rated wind speed scenario. The vertical lines correspond to the natural frequencies in surge (f_1) and yaw (f_6). The PSD of the Kaimal and TIMESR models, for T2, shows, in general, a quasi-static response; however, there is some response around the natural frequency in yaw, which is not seen for T1, for these two models. This resonant response is related to the non-zero energy content in the PSD of the y_c close to these frequencies. The Mann model shows a generally higher response for T1 compared to the other models, due to a lower coherence; however, the yaw response for T2 is lower than for the TIMESR and Kaimal models, due to the previously mentioned reasons. The trends described based on Figure 12, for unstable conditions, apply to stable and neutral conditions. Jacobsen and Godvik[54] analyzed the influence of wakes and atmospheric stability on the pitch and yaw of the Hywind spar and the results are broadly consistent. It can thus be concluded that the mean yaw of the turbine in the wake is mainly affected by shear and wake deficit, whereas the standard deviation is strongly affected by coherence, which directly affects wake meandering and depends on atmospheric stability.

5.2 | Structural response at the tower base, the blade root and the upwind mooring line fairlead

Figure 13 presents the average of the mean of the six realizations for the tower base fore-aft bending moment (TBFABM), top row, and the tension at fairlead 1 (FL1T), bottom row, plus-minus the average of the standard deviations for the six seeds, for every condition. To compute the standard deviation, a transient of 1000 s is removed, so the results presented are based on 1-h long time-series, and the entire frequency-range is
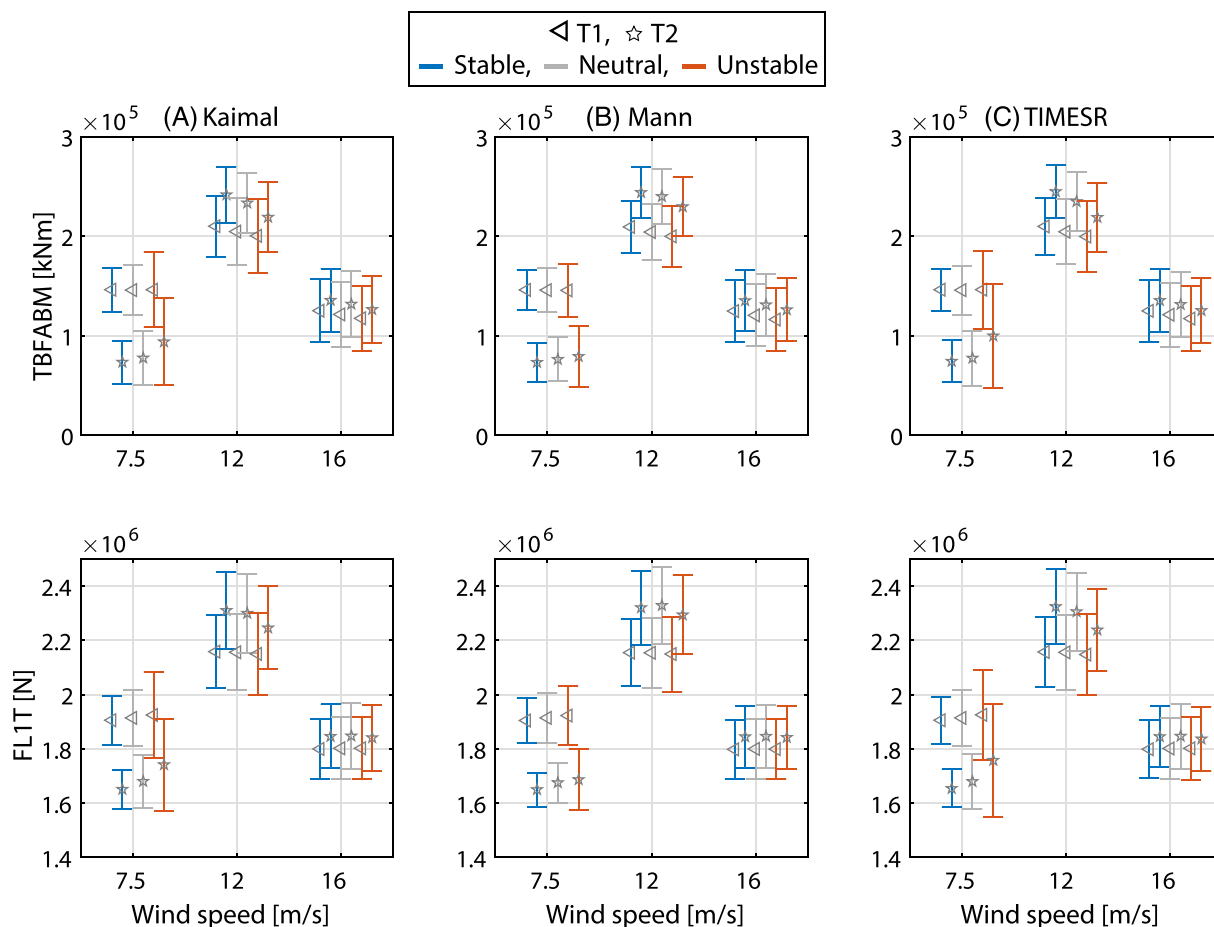

FIGURE 13 Average of the mean of the six realizations for the TBFABM (top row) and the FL1T (bottom row), plus-minus the average of the standard deviation for the six realizations, for each mean wind speed and stability condition, and for T1 (triangles) and T2 (stars). Column (A) is for the Kaimal model, column (B) for the Mann model, and column (C) for the TIMESR model.

included. The difference in mean values for both the TBFABM and FL1T is affected by the thrust that T1 and T2 experience. The trends observed are the same as the ones for the difference in the mean pitch. The lowest difference is seen in unstable conditions, due to a higher wake recovery rate. The standard deviation of the TBFABM and FL1T for both turbines is the highest for the TIMESR model in unstable conditions, and the difference between T1 and T2 follows the same trend as for pitch. For the above-rated wind speed scenario, the differences in the FL1T and TBFABM standard deviation between the two turbines are small, i.e. less than 5%. For the below-rated scenario, the standard deviation of the FL1T decreases for T2, except in unstable conditions, for which it increases up to 25% for the TIMESR model. The reason for this increase for the TIMESR model, and the relatively smaller decrease for this model and for Kaimal for stable and neutral conditions, compared to the Mann model, is the higher meandering due to a larger coherence for TIMESR and Kaimal. This reasoning is also the cause for the difference in the TBFABM standard deviations. The difference between T1 and T2 for the below-rated wind speed scenario reaches 33% for the unstable case, for the TIMESR model.

Figure 14 presents the average of the mean of the six realizations for the tower top yaw moment (TTYM), top row, and the blade-root out-of-plane moment (BROoPM), bottom row, for every condition. Both the difference in mean and standard deviation of the TTYM are reduced with the increase in mean wind speed. They are both highly correlated to the structure yaw, and therefore the same effect as reported before related to shear applies to the analysis on the mean TTYM. Even though the highest absolute values of the TTYM standard deviation are seen in unstable conditions for both T1 and T2, the largest difference in percentage between T1 and T2 is seen for neutral and stable conditions, for the below-rated wind speed scenario, for which T2 experiences a TTYM of more than twice the one of T1. For the close-to-rated wind speed scenario, in unstable conditions, the standard deviation of TTYM for T2 is 1.5 to 2 times the value for T1. In neutral conditions the difference lies between 35%, for the Mann model, and 70%, for the Kaimal model. The small difference for the Mann model is consistent with the smaller difference in yaw standard deviation for this model, compared to Kaimal and TIMESR, for the same reasons. The standard deviation of the TTYM is correlated to shear and wake meandering, which intrinsically depends on coherence. The trends seen here are lower than, but consistent with, the ones reported by Ning et al,[55] who used LES to study the effect of wake meandering in unstable and neutral conditions for the NREL 5MW, for rated wind speed. They found that in neutral conditions, the standard deviation of the TTYM of T2, placed 7 D downwind, was more than double the one of T1, and in unstable conditions, it was more than three times that of T1.

The mean values of the BROoPM for T1 and T2 follow the same trend as the mean values for pitch or the tower base fore-aft bending moment. The difference between T1 and T2 for the standard deviation depends mainly on the stability condition and mean wind speed. For the
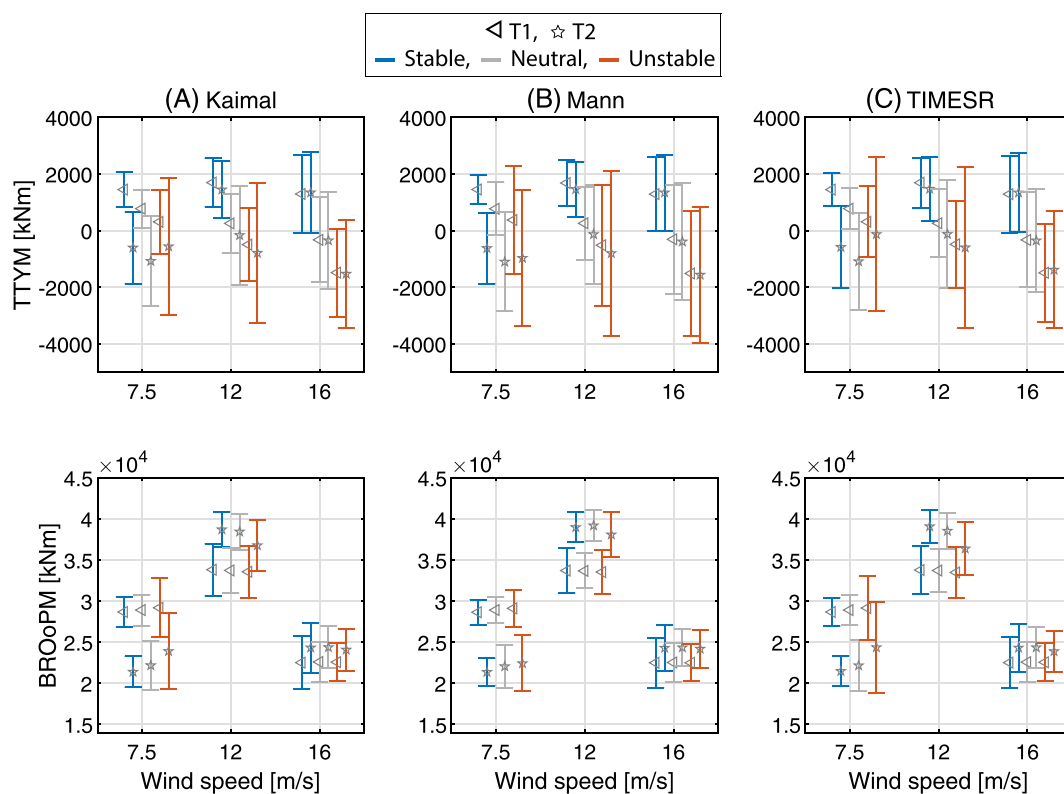

FIGURE 14 Average of the mean of the six realizations for the TTYM (top) and the BROoPM (bottom), plus-minus the average of the standard deviation for the six realizations, for each mean wind speed and stability condition, and for T1 and T2. Column (A) is for Kaimal, column (B) for the Mann model, and column (C) for the TIMESR model.

below-rated scenario, the highest difference is seen in unstable and neutral conditions, for which up to 35% increase is seen for T2. For the close-to-rated wind speed scenario, the difference is smaller. In stable conditions, the standard deviation for T2 is approximately 30% smaller than for T1, regardless of the model, whereas in unstable conditions the difference between T1 and T2 is negligible. For the above-rated wind speed scenario, the standard deviation is very similar between models or stability conditions. The standard deviation of the BROoPM is mainly affected by shear and wake deficit. The differences found in this work are smaller compared to the ones reported by Ning et al[55] regarding the standard deviation of the BROoPM. They found that for T2 the BROoPM standard deviation was 44% higher than the one of T1 in neutral conditions, and two times higher in unstable conditions.

6 | CONCLUSIONS

Since 2019, the dynamic wake meandering model has been included in the revised IEC 61400-1 standard[10] as a recommended practice to account for wake effects from neighboring turbines in a wind farm. This model represents a good compromise between the higher computational cost that high-fidelity models imply, and the lower accuracy of analytical wake models. Furthermore, IEC guidelines recommend two wind turbulence models for the design and analysis of FWTs. These turbulence models are based on neutral atmospheric conditions and do not account for the effects of non-neutral atmospheric conditions on coherence, turbulence intensity and mean shear on the wind profile. In this work, the combined effect of dynamic wake meandering and atmospheric stability, is studied on the response of the INO WINDMOOR 12 MW semisubmersible floating wind turbine[21] placed 8 D downwind in the wake. To account for atmospheric stability in the Kaimal and Mann methods, their input parameters are fitted to LES data. A third method, TIMESR, which allows the generation of the turbulent wind fields based on input time-series from LES, is used. The turbulent wind fields are input to FAST.Farm (which has the DWM model implemented), and OpenFAST 3.0 is used to study the low-frequency motions and structural response of the two INO WINDMOOR 12 MW FWTs, for stable, neutral, and unstable atmospheric conditions.

The wake deficit and meandering, influenced by atmospheric stability, play an important role in the motions and structural response of the FWT in the wake, T2. Four main conclusions can be drawn based on the current work:

- Wake recovery is greater for higher wind speeds and unstable conditions, and the effect of this greater recovery is clear in the mean pitch and in the mean tower base fore-aft bending moment, the upwind fairlead tension and the blade root out-of-plane moment signals, all of which are related to the increased or reduced thrust.
- The yaw motion and the tower top yaw moment mean values are mainly affected by shear, which is highest in stable conditions. The standard deviation in every motion and structural response is mostly influenced by meandering, which is highly correlated with lateral coherence.
- The largest difference between T1 and T2 for the responses related to yaw, where significant effects of wake deficit and meandering are seen, occurs for the TIMESR and Kaimal models. These differences are exacerbated because the yaw-related responses for T1 are low compared with Mann, which is consistent with literature,[19,56–58] compounded with the fact that there is increased meandering due to the higher coherence for Kaimal and TIMESR. This effect takes place especially for the below-rated wind speed scenario and unstable conditions, when meandering is highest, due to lower longitudinal wind speed components compared to the close-to-rated and above-rated cases.
- The effect of the wind turbulence model on the mean value of the turbine in the wake motions and structural response analyzed in this work is negligible. The standard deviation of T2 motions and structural response is affected by the wind turbulence model, especially in unstable conditions, due to the difference in coherence, and therefore wake meandering, of the three models studied here.

Both wake deficit and meandering, combined with the effect of atmospheric stability and the wind turbulence model play an important role at the lower-frequency range, where semisubmersible structures have their natural periods for rigid body motions. More specifically, coherence, directly affected by atmospheric stability, is one of the most important parameters influencing the wake meandering and FWTs response, both in the wake and in free wind. However, there is a lack of data regarding coherence, especially offshore and in the lateral direction, and regarding wake meandering. Accordingly, there are two main recommendations derived from the current work, and supported by other authors[59,60]:

- There is the need to overcome the scarcity of data regarding the spatial variation of the wind fields, especially in the areas where FWTs are likely to operate.
- Further validation of the mid-fidelity DWM model for floating wind turbines, with increasing rotor sizes, against higher fidelity models is needed.

PEER REVIEW

The peer review history for this article is available at https://www.webofscience.com/api/gateway/wos/peer-review/10.1002/we.2867.

DATA AVAILABILITY STATEMENT

Data requests will, within reason, be met by contacting Erin E. Bachynski-Polić on e-mail erin.bachynski@ntnu.no.

ORCID

Irene Rivera-Arreba 🆔 https://orcid.org/0000-0003-2258-7028

Erin E. Bachynski-Polić 🆔 https://orcid.org/0000-0002-1471-8254

REFERENCES

1. Ainslie JF. Calculating the flow field in the wake of wind turbines. *J Wind Eng Ind Aerodyn*. 1988;27(1-3):213-224. https://doi.org/10.1016/0167-6105(88)90037-2

2. Nybø A, Nielsen FG, Reuder J, Churchfield MJ, Godvik M. Evaluation of different wind fields for the investigation of the dynamic response of offshore wind turbines. *Wind Energy*. 2020;23(9):1810-1830. https://doi.org/10.1002/we.2518

3. Cheynet E, Flügge M, Reuder J, et al. The COTUR project: remote sensing of offshore turbulence for wind energy application. *Atmos Meas Tech*. 2021; 14(9):6137-6157. https://doi.org/10.5194/amt-14-6137-2021

4. Sathe A, Gryning S-E, Peña A. Comparison of the atmospheric stability and wind profiles at two wind farm sites over a long marine fetch in the north sea. *Wind Energy*. 2011;14(6):767-780. https://doi.org/10.1002/we.456

5. Barthelmie RJ. The effects of atmospheric stability on coastal wind climates. *Meteorol Appl*. 1999;6(1):39-47. https://doi.org/10.1017/s1350482799000961

6. Churchfield M, Wang Q, Scholbrock A, Herges T, Mikkelsen T, Sjöholm M. Using high-fidelity computational fluid dynamics to help design a wind turbine wake measurement experiment. *J Phys Conf Ser*. 2016;753:32009. https://doi.org/10.1088/1742-6596/753/3/032009

7. Keck RE, de Maré M, Churchfield MJ, Lee S, Larsen G, Madsen HA. Two improvements to the Dynamic Wake Meandering model: including the effects of atmospheric shear on wake turbulence and incorporating turbulence build-up in a row of wind turbines. *Wind Energy*. 2015;18:111-132. https://doi.org/10.1002/we.1686

8. Abkar M, Porté-Agel F. Influence of atmospheric stability on wind-turbine wakes: a large-eddy simulation study. *Phys Fluids*. 2015;27(3):35104. https://doi.org/10.1063/1.4913695

9. Larsen GC, Madsen HA, Thomsen K, Larsen TJ. Wake meandering: a pragmatic approach. *Wind Energy*. 2008;11(4):377-395. https://doi.org/10.1002/we.267

10. IEC. IEC61400-1: Wind Energy Generation Systems-Part 1: Design Requirements, Geneva, Switzerland, International Electrotechnical Commission; 2019.

11. Larsen TJ, Hansen AM. How to HAWC2, the User's Manual, Roskilde, Denmark, Risø National Laboratory; 2007.

12. Jonkman JM, Annoni J, Hayman G, Jonkman B, Purkayastha A. Development of FAST.Farm: a new multi-physics engineering tool for wind-farm design and analysis. In: American Institute of Aeronautics and Astronautics; 2017.

13. Madsen HA, Larsen GC, Larsen TJ, Troldborg N, Mikkelsen R. Calibration and validation of the dynamic wake meandering model for implementation in an aeroelastic code. *J Solar Energy Eng*. 2010;132(4):041014.

14. Larsen TJ, Madsen HA, Larsen GC, Hansen KS. Validation of the dynamic wake meander model for loads and power production in the Egmond aan Zee wind farm. *Wind Energy*. 2012;16(4):605-624. https://doi.org/10.1002/we.1563

15. Jonkman J, Doubrawa P, Hamilton N, Annoni J, Fleming P. Validation of FAST.Farm against large-eddy simulations. *J Phys Conf Ser*. 2018;1037:62005. https://doi.org/10.1088/1742-6596/1037/6/062005

16. Doubrawa P, Annoni JR, Jonkman JM. Optimization-based calibration of FAST.Farm parameters against large-eddy simulations. In: American Institute of Aeronautics and Astronautics; 2018.

17. Shaler K, Jonkman J, Hamilton N. Effects of inflow spatiotemporal discretization on wake meandering and turbine structural response using FAST. Farm. *J Phys Conf Ser*. 2019;1256:12023. https://doi.org/10.1088/1742-6596/1256/1/012023

18. Reinwardt I, Schilling L, Steudel D, Dimitrov N, Dalhoff P, Breuer M. Validation of the dynamic wake meandering model with respect to loads and power production. *Wind Energy Sci*. 2021;6(2):441-460. https://doi.org/10.5194/wes-6-441-2021

19. Wise AS, Bachynski EE. Wake meandering effects on floating wind turbines. *Wind Energy*. 2019;23(5):1266-1285. https://doi.org/10.1002/we.2485

20. Rivera-Arreba I, Wise AS, Hermile M, Chow FK, Bachynski-Polić EE. Effects of atmospheric stability on the structural response of a 12 MW semisubmersible floating wind turbine. *Wind Energy*. 2022;25:1917-1937. https://doi.org/10.1002/we.2775

21. Souza CE, Engebretsen E, Bachynski-Polić E, Eliassen L, Berthelsen P, Haslum H. Definition of the INO WINDMOOR 12 MW Base Case Floating Wind Turbine. *Technical Report*, Trondheim, Norway, SINTEF Ocean; 2021.

22. Bundesamt für Seeschifffahrt und Hydrographie. FINO - Databankinformationen; 2020.

23. Jonkman BJ. Openfast Documentation Release v2.1.0, Boulder, Colorado, NREL; 2019.

24. Jonkman BJ, Buhl M. TurbSim User's Guide, Boulder, Colorado, NREL; 2005.

25. DTU Wind Energy. Pre-Processing Tools—hawc2. *Technical Report*, Copenhagen, Denmark, Technical University of Denmark; 2014.

26. Maré dM, Mann J. Validation of the Mann spectral tensor for offshore wind conditions at different atmospheric stabilities. In: TORQUE; 2014.

27. Chougule A, Mann J, Kelly M, Larsen GC. Simplification and validation of a spectral-tensor model for turbulence including atmospheric stability. *Bound-Layer Meteorol*. 2018;167(3):371-397. https://doi.org/10.1007/s10546-018-0332-z

28. Skamarock WC, Klemp JB, Dudhia J, et al. A Description of the Advanced Research WRF Model Version 4, Boulder, CO, United States, UCAR/NCAR; 2019.

29. Kvittem MI, Moan T. Time domain analysis procedures for fatigue assessment of a semi-submersible wind turbine. *Mar Struct*. 2015;40:38-59. https://doi.org/10.1016/j.marstruc.2014.10.009

30. Li L, Gao Z, Moan T. Joint environmental data at five european offshore sites for design of combined wind and wave energy devices. In: American Society of Mechanical Engineers; 2013.

31. Keck RE. A consistent turbulence formulation for the dynamic wake meandering model in the atmospheric boundary layer. *Ph.D. Thesis*. Denmark: DTU Wind Energy PhD; 2013.

32. Branlard E, Martínez-Tossas LA, Jonkman J. A time-varying formulation of the curled wake model within the FAST.farm framework. *Wind Energy*. 2022;26(1):44-63. https://doi.org/10.1002/we.2785

33. Haupt SE, Kosović B, Shaw W, et al. On bridging a modeling scale gap: mesoscale to microscale coupling for wind energy. *Bull Am Meteorol Soc*. 2019; 100(12):2533-2550. https://doi.org/10.1175/BAMS-D-18-0033.1

34. Irwin JS. A theoretical variation of the wind profile power-law exponent as a function of surface roughness and stability. *Atmos Environ (1967)*. 1979; 13(1):191-194. https://doi.org/10.1016/0004-6981(79)90260-9

35. Emeis S. Current issues in wind energy meteorology. *Meteorol Appl*. 2014;21(4):803-819. https://doi.org/10.1002/met.1472

36. Kaimal JC, Wyngaard JC, Izumi Y, Coté OR. Spectral characteristics of surface-layer turbulence. *Q J R Meteorol Soc*. 1972;98(417):563-589. https://doi.org/10.1002/qj.49709841707

37. Davenport AG. The response of slender, line-like structures to a gusty wind. *Proc Inst Civ Eng Transp*. 1962;23(3):389-408. https://doi.org/10.1680/iicep.1962.10876

38. Taylor GI. The spectrum of turbulence. *Proc. R. Soc. London. Series A - Math Phys Sci*. 1938;164(919):476-490. https://doi.org/10.1098/rspa.1938.0032

39. Mann J. The spatial structure of neutral atmospheric surface-layer turbulence. *J Fluid Mech*. 1994;273:141-168. https://doi.org/10.1017/s0022112094001886

40. Cheynet E. Numerical implementation of the uniform shear model. https://github.com/ECheynet/MannModel1994/releases/tag/v1.7; 2021.

41. Welch P. The use of fast fourier transform for the estimation of power spectra: a method based on time averaging over short, modified periodograms. *IEEE Trans Audio Electroacoustics*. 1967;15(2):70-73. https://doi.org/10.1109/tau.1967.1161901

42. Cheynet E, Jakobsen JB, Reuder J. Velocity spectra and coherence estimates in the marine atmospheric boundary layer. *Bound-Layer Meteorol*. 2018; 169(3):429-460. https://doi.org/10.1007/s10546-018-0382-2

43. Chougule A, Mann J, Kelly M, Larsen GC. Modeling atmospheric turbulence via rapid distortion theory: spectral tensor of velocity and buoyancy. *J Atmos Sci*. 2017;74(4):949-974. https://doi.org/10.1175/jas-d-16-0215.1

44. Veers P. Modeling stochastic wind loads on vertical axis wind turbines. In: 25th structures, structural dynamics and materials conference AIAA; 1984.

45. Simon JS, Zhou B, Mirocha JD, Chow FK. Explicit filtering and reconstruction to reduce grid dependence in convective boundary layer simulations using WRF-LES. *Mon Weather Rev*. 2019;147(5):1805-1821. https://doi.org/10.1175/MWR-D-18-0205.1

46. Hirth BD, Schroeder JL, Guynes JG. Diurnal evolution of wind structure and data availability measured by the DOE prototype radar system. *J Phys Conf Ser*. 2017;926:12003. https://doi.org/10.1088/1742-6596/926/1/012003

47. Göçmen T, Larsén XG, Imberger M. The effects of open cellular convection on wind farm operation and wakes. *J Phys Conf Ser*. 2020;1618(6):62014. https://doi.org/10.1088/1742-6596/1618/6/062014

48. Silva de Souza CE, Bachynski-Polić EE. Design, structural modeling, control, and performance of 20 MW spar floating wind turbines. *Mar Struct*. 2022; 84:103182. https://doi.org/10.1016/j.marstruc.2022.103182

49. Jonkman J, Shaler K. Fast.farm user's guide and theory manual, Boulder, Colorado, NREL; 2021.

50. Quon EW, Doubrawa P, Debnath M. Comparison of rotor wake identification and characterization methods for the analysis of wake dynamics and evolution. *J Phys Conf Ser*. 2020;1452(1):12070. https://doi.org/10.1088/1742-6596/1452/1/012070

51. Doubrawa P, Sirnivas S, Godvik M. Effects of upstream rotor tilt on a downstream floating wind turbine. *J Phys Conf Ser*. 2021;1934(1):12016. https://doi.org/10.1088/1742-6596/1934/1/012016

52. Nanos EM, Bottasso CL, Manolas DI, Riziotis VA. Vertical wake deflection for floating wind turbines by differential ballast control. *Wind Energy Sci*. 2021;1934(2021):012016. https://doi.org/10.5194/wes-2021-79

53. Rivera-Arreba I, Li Z, Yang X, Bachynski-Polić E. Validation of the dynamic wake meandering model against large eddy simulation for horizontal and vertical steering of wind turbine wakes. arXiv; 2023.

54. Jacobsen A, Godvik M. Influence of wakes and atmospheric stability on the floater responses of the hywind scotland wind turbines. *Wind Energy*. 2020;24(2):149-161. https://doi.org/10.1002/we.2563

55. Ning X, Wan D. LES study of wake meandering in different atmospheric stabilities and its effects on wind turbine aerodynamics. *Sustainability*. 2019; 11(24):6939. https://doi.org/10.3390/su11246939

56. Doubrawa P, Churchfield MJ, Godvik M, Sirnivas S. Load response of a floating wind turbine to turbulent atmospheric flow. *Appl Energy*. 2019;242: 1588-1599. https://doi.org/10.1016/j.apenergy.2019.01.165

57. Bachynski EE, Eliassen L. The effects of coherent structures on the global response of floating offshore wind turbines. *Wind Energy*. 2019;22:219-238. https://doi.org/10.1002/we.2280

58. Nybø A, Nielsen FG, Godvik M. Sensitivity of the dynamic response of a multimegawatt floating wind turbine to the choice of turbulence model. *Wind Energy*. 2022;25(6):1013-1029. https://doi.org/10.1002/we.2712

59. Nielsen FG. Perspectives and challenges related offshore wind turbines in deep water. *Energies*. 2022;15(8):2844. https://doi.org/10.3390/en15082844

60. Veers P, Dykes K, Lantz E, et al. Grand challenges in the science of wind energy. *Science*. 2019;366(6464):eaau2027. https://doi.org/10.1126/science.aau2027